Modular structure of RNA 3' processing condensates involving the Arabidopsis RNA binding protein FCA

Geng-Jen Jang[1], Alex L. Payne-Dwyer[2,3], Robert Maple[1], Zhe Wu[1,4], Fuquan Liu[1,5], Sergio G. Lopez[1], Mark C. Leake[2,3] and Caroline Dean[1,*]

[1]Department of Cell and Developmental Biology, John Innes Centre, Norwich, UK

[2]School of Physics, Engineering and Technology, University of York, York, UK

[3]Department of Biology, University of York, York, UK

[4]Institute of Plant and Food Science, Southern University of Science and Technology, Shenzhen, China

[5]Institute of Global Food Security, School of Biological Sciences, Queen's University Belfast, Belfast, UK

*Corresponding author, Tel: +44 (0)1603 450000; E-mail: caroline.dean@jic.ac.uk

Keywords: biomolecular condensate, RNA processing, *FLC*, *COOLAIR*, noncoding RNA

Abstract

The Arabidopsis RNA binding protein FCA is found in liquid-like nuclear condensates and promotes proximal polyadenylation of specific nascent transcripts. To understand the *in vivo* interactions required for these condensates we used single-particle tracking experiments on FCA expressed at endogenous levels in live cells. These revealed FCA forms a core tetramer that multimerizes into higher-order particles (~16 to 56 FCA molecules), corresponding to condensates observed using confocal microscopy. The coiled-coil protein FLL2, genetically required for FCA function and condensate formation, showed co-localization primarily to the larger condensates. FCA regulates *FLC*, however, its *in vivo* co-localization with an *FLC lacO*/LacI transgene was found to be infrequent. A missense mutation in the FCA RRM domain showed RNA binding to FCA is necessary for function. This reduced RNA-binding activity, attenuated FCA condensate formation, 3' RNA processing and *FLC* repression, however it did not influence the core tetramer. Our work points to a modular structure for FCA condensates centred around a core of four FCA molecules, which multimerize to larger functionally important condensates via associated RNA and FLL2 interaction, with only transient residency at their site of action.

Introduction

Cellular compartmentalization by biomolecular condensates is associated with diverse processes in eukaryotic cells (Banani *et al*, 2017). While *in vitro* studies have highlighted their roles in increasing local concentration and residence time of interacting components, the functional characteristics of heterogeneous condensates *in vivo* remain unclear. Plants are an excellent system in which to study biomolecular condensates (Field *et al*, 2023). For example, Arabidopsis *FLOWERING LOCUS C* (*FLC*), a gene encoding a key flowering repressor, is regulated by co-transcriptional and antisense-mediated

chromatin silencing mechanisms (Fang *et al*, 2020; Xu *et al*, 2021) that involves multiple nuclear biomolecular condensates with very different properties (Zhu *et al*, 2021; Fiedler *et al*, 2022; Berry *et al*, 2017). One of those is a liquid-like condensate that involves an RNA-binding protein called FCA, which directly interacts with FY, a Pfs2p/WDR33 homologue and a central component of the polyadenylation machinery in eukaryotes (Simpson *et al*, 2003). FCA contains two RRM (RNA Recognition Motif) domains and a WW domain located between two predicted prion-like domains (Macknight *et al*, 1997). It was shown to form nuclear condensates through liquid-liquid phase separation and to recruit RNA 3' processing factors (Fang *et al*, 2019). Mutant screening identified a coiled-coil protein, FLL2, required for the liquid-liquid phase separation of FCA nuclear condensates and participation in *FLC* regulation (Fang *et al*, 2019). *In vitro* assays revealed that FCA condensates were enhanced by addition of low amounts of Arabidopsis RNA. However, the immunoprecipitation of *COOLAIR* nascent transcripts by FCA was not dependent on FLL2 (Fang *et al*, 2019).

We have continued our investigations of the properties of FCA liquid-like condensates and exploited a single-molecule imaging technique, using Slimfield microscopy with an oblique illumination angle of 60 ± 5°degrees to enhance imaging contrast (Plank *et al*., 2009). This enables simultaneous tracking of individual molecules within a wide range of biological condensates providing quantitative measurements of molecule number and molecular motion behavior in plant nuclei (Shen *et al*, 2023). It has been used to study biomolecular condensates in live cells including bacteria, yeast or mammalian cells (Kent *et al*, 2020; Izeddin *et al*, 2014; Ladouceur *et al*, 2020; Biswas *et al*, 2022) and we adapted it for living plant tissues to specifically study nuclear proteins (Bayle *et al*, 2021).

Our findings indicate that FCA condensates consist of multimers of a tetrameric FCA core, with sizes ranging from approximately 16 to 56 molecules. The lower diffusion coefficient of the larger particles, compared to core particles, suggests they correspond to the liquid-like condensates observed using confocal microscopy. Notably, FLL2, essential for FCA function, predominantly co-localizes within the larger condensates. However, sustained co-localization of large FCA condensates with the *FLC* locus is observed only infrequently. The involvement of RNA in promoting FCA condensation was shown through the identification of a missense mutation in the FCA second RRM domain. This mutation reduced RNA-binding activity *in vitro*, significantly attenuated FCA condensate formation, lowered RNA 3' processing efficiency and prevented *FLC* repression but did not influence the core tetramer. Our work points to a modular structure for FCA and RNA 3' processing condensates, with a core of four FCA molecules that multimerize via associated RNA and FLL2 interaction to larger functionally important condensates.

Results

Single-particle tracking reveals physical properties of FCA condensates.

Biomolecular condensates are considered to increase local concentration of its components (Banani *et al*, 2017; Shin & Brangwynne, 2017). To assess the consequence of condensation on FCA function, we generated plants carrying an FCA-mScarlet-I translational fusion. A mScarlet-I coding sequence was inserted into an FCA genomic clone and transgenic plant lines carrying single T-DNA insertion were generated, where the fusion was expressed at similar level as the endogenous FCA gene (Fig EV1A and B). The FCA mScarlet-I fusion formed liquid-like condensates (Fig 1A) and rescued the *fca-9* mutant phenotype (Fig EV1B). mScarlet-I is a bright red fluorescent protein known for its characteristics as a rapidly maturing monomer (Bindels *et al*, 2016) and using this in conjunction with the Slimfield microscope provided the capability to track very small FCA particles dynamically *in vivo* (Fig 1A). The single-molecule sensitivity of Slimfield *in vivo*, coupled with stepwise photobleaching of fluorescent protein tags (Leake *et al*, 2006; Reyes-Lamothe *et al*, 2010), also enabled accurate quantification of the number of molecules (stoichiometry) within the condensate (EV2; Jin *et al*, 2021).

Analysis of the single-particle tracking dataset identified a distinct peak representing approximately 4 molecules of FCA (Fig 1B) with other peaks in multiples of 4 from approximately 16 to 56 molecules. To investigate whether these regular peaks follow specific patterns, we conducted simulations through kernel density estimation to assess their periodicity (Leake *et al*, 2008). The estimate of the number of molecules in a repeat unit depends on consistent stoichiometry intervals observed between nearest-neighbor peaks in the stoichiometry distribution. The periodicity peaks for FCA particles were found to be approximately 4.2 and 8.7 (Fig 1C).

Particles can also exhibit different motion behaviour (Shen *et al*, 2023). We analysed the diffusion coefficient of individual particles and plotted single particles with stoichiometry. Generally, particles with low stoichiometry display variable mobility, while those with high stoichiometry show low mobility (Fig 1D). These results suggest that the core module of an FCA particle is a tetramer with larger condensates forming through the higher-order assembly of these tetrameric cores.

The co-localization of FCA and FLL2 is primarily observed in the prominent foci in Arabidopsis.

Our previous study used transient assays suggested that FCA condensates serve as the sites for the interaction between FCA, FLL2 and 3'-end processing factors (Fang *et al*, 2019). However, the condensates formed by FCA and FLL2 exhibited different patterns in low resolution images of Arabidopsis roots (Fang *et al*, 2019). To investigate the potential co-localization of FCA and FLL2 within the same nuclear condensates *in vivo*, we crossed plants carrying an FCA-mTurquoise2 transgene (Xu *et al*, 2021) with plants carrying FLL2-eYFP transgene (Fang *et al*, 2019) and generated double homozygotes. Utilizing 3D imaging and Airyscan confocal microscopy, we found that FCA and FLL2

generally reside in distinct fluorescent foci within the cell nucleus (Fig 2A) but co-localize within a few larger foci (Fig 2B and D). We conducted a comprehensive analysis to determine the size distributions for FCA, FLL2 and FCA/FLL2-co-localized condensates (Fig 2C). The data suggest a specific association between FCA and FLL2 within larger condensates.

To determine if these prominent FCA/FLL2 condensates directly associate with the *FLC* locus, we crossed the FCA-mScarlet-I transgene into a line carrying a previously established *FLC-lacO*/LacI-eYFP system that enables spatial localization of the *FLC* locus in the nucleus (Rosa *et al*, 2013). FCA condensates did not frequently co-localize with the *FLC-lacO*/LacI-eYFP marked locus (Fig EV3). Only 2.7% of identified FCA condensates partially co-localized with the *FLC-lacO*/LacI-eYFP locus suggesting that FCA condensates only transiently associate with the *FLC* locus.

FCA condensation is dependent on a functional RRM domain.

To further investigate the functional significance of the heterogeneity in FCA condensates we continued a genetic screen for factors essential for FCA function (Liu *et al*, 2007). This identified a missense mutation on the FCA overexpression transgene at amino acid 304 of the FCA protein, resulting in a leucine to phenylalanine change (Fig EV1C). This alteration is located within the second RRM domain of FCA, a domain conserved across various species (Macknight *et al*, 1997). The impact of this missense mutation on the RNA-binding activity was established through *in vitro* RNA-binding assays (Fig EV1D). That the mutant came out of an *FLC* mis-expression screen and exhibited late flowering shows the RNA-binding activity is important for FCA function (Fig EV1E).

To examine whether this RRM mutation affects FCA condensation, we generated transgene constructs expressing an FCA wild-type genomic DNA fragment with (FCArrm) and without (FCAwt) the RRM mutation fused with mScarlet-I and introduce them into *fca-9* mutant (Fig EV1A). After selecting for single insertion transgenic plants and homozygotes, we analysed the FCAwt condensates within the nuclei of young roots using Airyscan confocal microscope. Plants containing the FCArrm transgene limited the size and number of condensates, displaying a more diffuse signal compared to plants carrying FCAwt (Fig 3A and B).

In order to determine whether the RRM mutant alters the structure of FCA condensates, we also conducted single-particle tracking with the FCArrm lines. We observed an obvious stoichiometry peak of approximately 4 molecules for FCArrm, slightly higher than that for FCAwt (Fig 3C; Appendix Fig S1). However, when focusing on particles with stoichiometries exceeding 8 molecules, the probability density of FCArrm was found to be lower than FCAwt. FCArrm particles with more than 16 molecules were scarce, however, the integrated nuclear intensity of fluorescent signal in FCArrm and FCAwt showed no obvious change (Appendix Fig S2). This result suggests that the reduced RNA-binding

activity of FCA proteins decreases their likelihood of forming larger particles with a range of 16 to 56 molecules, consistent with the confocal imaging analysis.

To determine if the RRM mutant changed the physical properties of FCA condensates, we compared the diffusion coefficients of individual particles with their stoichiometry (Fig 3D). The mean stoichiometry of FCArrm is lower than that of FCAwt, while the overall pattern of diffusion coefficients is distributed towards slightly higher values (Fig 3E; Appendix Fig S3). Surprisingly, the periodic unit of FCArrm only experiences a minor reduction compared to FCAwt, which implies that FCA proteins with reduced RNA-binding activity retain the capacity to form the tetrameric core (Fig 3F). Thus, the RNA-binding activity of FCA proteins affects the formation of larger condensates but does not affect core protein assembly.

The functional RNA-binding domain is required for *COOLAIR* R-loop resolution and FCA auto-regulation.

We then used the FCAwt and FCArrm lines to further investigate the functional importance of RNA binding. Compared to the FCAwt transgenic plants, FCArrm plants displayed higher levels of *FLC* expression and therefore flowered late (Fig 4A and B, EV1B). FCA associates with *COOLAIR*, recruiting 3' processing factors to promote proximal *COOLAIR* polyadenylation, thus resolving a *COOLAIR*-formed R-loop (Liu *et al*, 2010; Xu *et al*, 2021). The ratio of proximal-to-distal isoforms of *COOLAIR* transcripts was reduced in the FCArrm lines compared to FCAwt consistent with reduced R-loop resolution when RNA binding is defective (Fig 4C). S9.6-DNA/RNA immunoprecipitation followed by cDNA conversion (DRIPc)-qPCR analysis also revealed FCArrm has reduced ability to resolve the *COOLAIR*-induced R-loop (Fig 4D).

FCA autoregulates itself promoting polyadenylation at the proximal sites in intron3 (Quesada *et al*, 2003), so we conducted Quant-seq analysis to capture polyadenylated *FCA* transcripts in Col-0, FCAwt, FCArrm and *fca-9.* In FCArrm and *fca-9*, there were significantly fewer reads of transcripts corresponding to proximally polyadenylated *FCA* transcripts compared to Col-0. Conversely, reads at the distally polyadenylated site of *FCA* increased (Fig 4E-F), all consistent with reduced FCA function. RNA-binding activity is thus important for FCA condensation and for well-defined FCA functional roles, promotion of proximal *COOLAIR* termination and R-loop resolution.

Discussion

Our study provides insight on the functional properties of the dynamic liquid-like RNA 3' processing condensates containing the Arabidopsis nuclear RNA-binding protein FCA. We conducted single-particle tracking to determine the molecular stoichiometry and diffusivity of FCA condensates in plant nuclei. This revealed insights into the particle assembly size and association of FCA with its protein

187 and RNA partners functioning in *FLC* repression. Our work points to a modular structure for FCA
188 condensates centred around a core of four FCA molecules, which multimerize to larger functionally
189 important condensates via associated RNA and FLL2 interaction, with only transient residency at their
190 site of action.
191
192 The missense mutation in the FCA RRM domain reduced RNA-binding activity, attenuated condensate
193 formation and prevented *FLC* repression but the stoichiometry of the smaller FCA particles was
194 unaffected. The lack of effect of RNA binding on the core modular structure is similar to previous
195 observations with ELAV, a well-characterized RNA-binding protein with three RRM domains. ELAV
196 multimerizes on its target RNAs and forms a defined complex (Soller & White, 2005). Future analysis
197 should examine how FCA core tetramers multimerize. The FCA prion-like domain (Chakrabortee *et al*,
198 2016), RRM domain (Macknight *et al*, 1997), WW domain (Simpson *et al*, 2003; Henderson *et al*, 2005)
199 and extended NH2 terminus initiating in a non-methionine start codon (Simpson *et al*, 2010) may all
200 play a role. In addition, m6A exerts function in the regulatory mechanisms of *FLC* and *COOLAIR* (Xu
201 *et al*, 2021; Wang *et al*, 2022; Sun *et al*, 2022; Amara *et al*, 2023); we need to understand if the dynamic
202 structures are affected by RNA modification and how this tetramer interfaces with its target RNAs.
203 Continued analysis of the role of the first RRM may also be productive as the protein phosphatase
204 SSU72 was found to antagonize FCA's binding to *COOLAIR* in a manner dependent on the first RRM
205 motif (Yongke Tlan *et al*, 2019).
206
207 *COOLAIR* transcripts form dense 'clouds' at each *FLC* locus as judged by single-molecule fluorescence
208 in situ hybridization, which are enhanced upon cold exposure (Rosa *et al*., 2016). Whether the FCA
209 condensates associate with these RNA condensates will require RNA live imaging analysis. It is
210 interesting to speculate that *COOLAIR* molecules might undergo thermo-responsive phase transitions
211 as has been found recently for other RNAs (Wadsworth *et al*., 2023). Protein partners can tune this
212 phase behaviour (Ruff *et al*., 2020), so this system has a lot of potential to uncover fundamental
213 principles of condensate functionality *in vivo,* and if transient association with the *FLC* locus is
214 sufficient for function. In mammalian cells, Mediator-bound enhancers only sporadically co-localize
215 with their target loci. This variability in co-localization can be attributed to a dynamic kissing model,
216 where a distal Mediator cluster interacts with the gene only at specific timepoints (Cho *et al*, 2018).
217
218 Our work demonstrates the power of studying biomolecular condensate functionality in genetically
219 tractable systems. Arabidopsis with its extensive genetic resources, ability to make transgenic lines and
220 small, transparent roots is particularly suitable for these studies, as illustrated by our ability to image
221 condensates in living roots with the single-molecule sensitivity of Slimfield. Coupled with stepwise
222 photobleaching we could accurately quantify the number of molecules within condensates providing
223 mechanistic insights into the modular structure of FCA condensates, with and without various

224 functionally important partners. These tools now allow us to explore the role of FCA condensate
225 dynamics in response to various environmental exposures.
226
227 **Materials and Methods**
228
229 **Plant materials and growth conditions**
230 The wild type Col-0, *fca-9* mutant allele, *pFCA::FCA-mTurquoise* and *pFLL2::FLL2-eYFP* transgenic
231 plants were described previously (Fang *et al*, 2020; Xu *et al*, 2021). To generate the pFCA::FCA-
232 mScarlet-I transgenic plants, FCA genomic DNA fragments was amplified and insert into the pENTRY
233 vector. The mScarlet-I coding sequence was inserted before the stop codon via In-Fusion seamless
234 cloning. The FCA genomic DNA fragment fused mScarlet-I was transferred to pSLJ699I5 vector via
235 gateway cloning. The RRM mutation construct is modified from wild-type FCA genomic DNA
236 constructs via In-Fusion seamless cloning. These constructs were transformed into the *fca-9* mutant.
237 Arabidopsis seeds were surface sterilized and sown on standard half-strength Murashige and Skoog (½
238 MS) medium plate without glucose and stratified at 4 °C for 3 days before transferred to long-day
239 conditions (16-h light at 20 °C, 8-h darkness at 16 °C).
240
241 **Confocal microscopy of FCA-mScarlet-I**
242 Plants were grown vertically on half strength MS plates for 4-7 days. Confocal images were acquired
243 on a Zeiss LSM 880 upright microscope equipped with an Airyscan detector. Samples were imaged
244 through a C-Apochromat 63x/NA 1.2 water-immersion objective by exciting them at 561 nm and using
245 the Airyscan detector in super resolution mode. The fluorescence emission arrived at the detector after
246 passing through a filter that allowed wavelengths between 495-550 nm and above 570 nm to pass
247 through. The voxel size was 0.06 × 0.06 × 0.26 µm (xyz) and the pixel dwell time was 1.78 µs. Z-stacks
248 comprised 28 slices and spanned a 7.13 µm range. After Airyscan processing, the image analysis was
249 performed in Arivis Vision4D ver. 4.1.0. (Zeiss) as described below.
250
251 **Co-localization analysis of FCA and FLL2**
252 Confocal images were acquired either on the Zeiss LSM 880 microscope mentioned above or a Zeiss
253 LSM 980 confocal microscope. For using LSM880, line by line sequential acquisition was employed.
254 Samples were imaged through a C-Apochromat 63x/NA 1.2 water-immersion objective and were
255 excited at 458 (mTurquoise) and 514 nm (eYFP). The fluorescence emission of the samples passed
256 through a filter that only allowed wavelengths in the 465-505 nm range and above 525 nm to reach the
257 Airyscan detector, which was operating in super resolution mode. The voxel size was 0.05 × 0.05 ×
258 0.21 µm (xyz) and the pixel dwell time was 0.72 µs. Z-stacks comprised 25 slices spanning a 4.96 µm
259 range. 0.2 mm TetraSpeck microspheres (Thermo Fisher Scientific, UK) were imaged using these same
260 settings and the resulting images were used to correct the sample images for chromatic aberration. The
261 correction was performed in Zen (Zeiss, Germany) using the channel alignment method.

For using Zeiss LSM 980, frame by frame acquisition was employed. Samples were imaged through a C-Apochromat 63x/NA 1.2 water-immersion objective and were excited at 445 (mTurquoise) and 514 nm (eYFP). The fluorescence emission of eYFP was collected through a filter that only allowed wavelengths in the 530-582 range to reach the Airyscan detector, whereas the fluorescence emission of mTurquoise was collected through a filter that allowed wavelengths in the 422-497 and 607-735 nm ranges to reach the Airyscan detector. The detector was operating in super resolution mode. The voxel size was $0.05 \times 0.05 \times 0.20$ µm (xyz) and the pixel dwell time was 1.06 µs. Z-stacks comprised 30 slices spanning a 5.8 µm range.

After Airyscan processing, the image analysis was performed in Arivis Vision4D ver. 4.1.0. (Zeiss). Firstly, the blob finder algorithm was applied to the mTurquoise2 channel using a diameter value of 0.35 mm, a probability threshold of 60%, and a split sensitivity of 50%. Then, the blob finder algorithm was applied to the eYFP channel using a diameter value of 0.30 mm, a probability threshold of 50%, and a split sensitivity of 50%. Blob finder is a segmentation algorithm that excels at finding round or spherical objects in 2D or 3D, respectively. It uses a Gaussian scale to identify seeds for the objects and subsequently applies a watershed algorithm to determine the boundaries of the objects. Afterwards, the intersection between the output of the two blob finder operations was calculated. Finally, metrics such as volume, mean intensity, and total intensity were computed for the objects generated by each of the blob finder operations, as well as for their intersection.

Slimfield microscopy

The customized Slimfield microscope was previously described (Payne-Dwyer and Leake, 2022). Continuous wave lasers (Coherent OBIS) delivered a de-expanded Gaussian beam mode (TEM00) to the back aperture of an NA 1.49 Apo TIRF 100× oil immersion objective lens (Nikon). Single molecule sensitivity was achieved using a fast sCMOS camera (Photometrics Prime95B) which triggered a continuous wave laser for 10 ms exposure per frame at 80 Hz. Excitation and emission filters were tailored to mScarlet-I (594/25 nm) for their respective red channels. The total magnification was approximately 200×, resulting in an oversampled image pixel edge size of 53 nm. Nuclei were identified using brightfield mode to determine the best focus and were subsequently captured for manual segmentation later. Fluorescence acquisition settings in the green and red channels were pre-optimized to prevent initial saturation and to ensure the detection of individual molecular brightness tracks for mScarlet-I. These settings were then locked to prevent systematic variation in the characteristic single molecule brightness.

296 **Single-particle tracking and intensity analysis**

297 Fluorescent foci were identified from Slimfield image sequences and linked into tracks using
298 ADEMScode software (Plank *et al*, 2009). Each of these foci were localised to a super-resolved,
299 subpixel precision, typically 40 nm. The random overlap probability was estimated using a nearest
300 neighbour distance approach (Payne-Dwyer *et al*, 2023). Analysis was spatially restricted to data lying
301 within a region of effectively uniform laser illumination (80% ± 9% s.d. peak intensity) by cropping
302 images to an area of 240 × 184 pixels (12.7 × 9.8 μm). Fluorescence image sequences were further
303 cropped to specify individual nuclei, using manually segmented masks from brightfield images.
304 The 2D diffusion coefficient of each track (D) was computed using the increase of mean-square
305 displacement across time interval according to a random walk model (Leake *et al*, 2008). Focus
306 intensity was calculated by summing the pixel values within a 5-pixel distance and subtracting an
307 averaged background level from the rest of a 17-pixel square (Leake *et al*, 2008). The track
308 stoichiometry was found by extrapolating the first 5 foci intensities to account for photobleaching
309 (Syeda *et al*., 2019), then dividing this initial intensity by the characteristic single molecule brightness
310 (Wollman *et al*., 2017). The characteristic single molecule brightness linked to each reporter was
311 determined as 110 ± 15 (mean ± sem) for mScarlet-I based on the Chung-Kennedy-filtered terminal
312 intensity of tracks in each acquisition (Leake *et al*, 2003), thus providing an internal calibration for track
313 stoichiometry, periodicity, and nuclear protein copy number.
314
315 To calculate periodicity, the stoichiometries of all tracks within each nucleus were represented as a
316 kernel density distribution (Leake *et al*, 2014), employing an empirical standard deviation of 0.6
317 molecules on the characteristic single molecule brightness. Peaks within this distribution were identified
318 using the MATLAB *findpeaks* function, and the intervals between nearest neighbour peaks were
319 computed (Payne-Dwyer and Leake, 2022). Raw estimations of the total number of molecules in each
320 nucleus were determined using ImageJ macros to integrate the pixel values inside segmented nuclei as
321 in previous work (Wollman and Leake, 2015; Payne-Dwyer and Leake, 2022). The nuclear protein copy
322 number of each reporter dataset was refined to exclude autofluorescence by calculating the difference
323 between mean integrated nuclear intensities of the labelled dataset and an unlabeled control, adjusted
324 proportionally to the ratio of mean nuclear segment areas.
325
326 **Expression analysis**

327 Total RNA was extracted from plant materials as described previously (Qüesta *et al*, 2016), treated with
328 TURBO DNase (Ambion) to eliminate DNA contamination, and reverse-transcribed using SuperScript
329 IV Reverse Transcriptase (Invitrogen) with gene-specific reverse primers. Quantitative PCR (qPCR)
330 analysis was conducted on a LightCycler480 II (ROCHE), and the qPCR data were normalized to the
331 reference genes *UBC* and *PP2A*. To measure the proximal ratio of *COOLAIR*, the level of the proximal
332 component was normalized to the distal *COOLAIR*. Primers were listed in Appendix Table S1.

333

334 **DNA−RNA hybrid immunoprecipitation followed by cDNA conversion (DRIPc)**

335 The DRIP protocol is as described previously (Xu *et al*, 2021) with modifications. In all, 3 g 10-day-
336 old seedlings were harvested and grounded into a fine powder. The powder was suspended in 35 mL of
337 Honda buffer (20mM HEPES, 0.44M sucrose, 1.25% Ficoll, 2.5% dextran T40, 10mM $MgCl_2$, 0.5%
338 Triton x-100, 5 mM DTT, 1x protease inhibitor cocktail (Roche), filtered through one layer of Miracloth,
339 and centrifuged at 3500×g for 15 min. Nuclear pellets were resuspended in 1mL Honda buffer and
340 centrifuged at 8000×g for 1 min. Pellets were then resuspended in the lysis buffer (50mM Tris-HCl pH
341 8.0, 10mM EDTA, 1% SDS) supplied with 0.1 mg/mL proteinase K (AM2546, Invitrogen) and digested
342 at 55 °C overnight with gentle rotation. The mixture was phenol/chloroform extracted, followed by
343 nucleic acid precipitation with NaOAc and ethanol. The nucleic acid pellet was dissolved in water and
344 quantified with Qubit DNA quantification kit (Invitrogen). In general, 1 μg of nucleic acid was digested
345 by restriction enzymes including DdeI, NdeI and XbaI (NEB) overnight. The digested nucleic acid was
346 phenol/chloroform extracted, followed by nucleic acid precipitation with NaOAc and ethanol. Then the
347 nucleic acid was treated with RNAse III (Ambion) and then extracted by phenol/chloroform and ethanol
348 precipitation. The treated nucleic acid was then diluted ten times with dilution buffer (16.7mM Tris pH
349 7.5, 167mM NaCl, 2.2mM EDTA, 0.1% Triton X-100) and 10% was stored at −20 °C as input. In all,
350 5 μg of S9.6 antibody (1:100 dilution, ENH001, Kerafast) was added, then incubated overnight at 4 °C.
351 The next day, 50 μl Protein G Agarose (Invitrogen) was added and incubated for another 2 h. The
352 immunoprecipitants were washed five times with dilution buffer and twice with TE buffer, then were
353 eluted in 100 μl elution buffer (10mM Tris pH 7.5, 2 mM EDTA, 0.2% SDS, 100 ng/μl tRNA) at 55 °C
354 for 2 hours, together with input samples. The nucleic acids were precipitated with NaOAc, isopropanol,
355 and glycogen, dissolved in water. The nucleic acid samples were then treated with treated with TURBO
356 DNase (Ambion) to eliminate DNA contamination, and reverse-transcribed using SuperScript IV
357 Reverse Transcriptase (Invitrogen) with gene-specific reverse primers. All the samples including inputs
358 were subjected to qPCR analysis via LightCycler480 II (Roche). The data were normalized to 1% of
359 input. Primers were listed in Appendix Table S1.

360

361 **Quant-seq**

362 The Quant-seq protocol is as described previously (Mateo-Bonmatí *et al*, 2024). The total RNAs
363 prepared for Quant-seq underwent purification using the Qiagen RNeasy miniprep kit (74106). Lexogen
364 GmbH (Austria) conducted the library preparation, sequencing, and data analysis. Sequencing-ready
365 libraries were created from 100 ng of input RNA using a QuantSeq 3' mRNA-Seq Library Prep Kit
366 REV for Illumina (015UG009V0271), following standard procedures. The RNA integrity and quality
367 of indexed libraries were assessed on a Fragment Analyzer device (Agilent Technologies) using a DNF-
368 471 RNA Kit and HS-DNA assay, respectively. Library quantification was carried out using a Qubit
369 dsDNA HS assay (Thermo Fisher).

370 A sequencing-ready pool of indexed libraries was then sequenced on an Illumina NextSeq 2000 with a
371 100-cycle cartridge, using the Custom Sequencing Primer (CSP). Verification of read quality utilized
372 FastQC version v0.11.7, and read adapter trimming employed cutadapt version 1.18 (Martin 2011).
373 Clean reads were mapped to the latest version of the Arabidopsis genome (TAIR10) using the splice-
374 aware aligner STAR version 2.6.1a (Dobin *et al*, 2013). The raw reads have been deposited in the Short
375 Read Archive (SRA) under the reference (PRJNA1087342 and PRJNA1076161).
376
377 **Electrophoretic Mobility Shift Assay**
378 FCA cDNA with L304F mutation was amplified from the mutant as described in Figure EV1.
379 To generate RNA probes, dsDNA of the corresponding region was amplified through PCR (primers see
380 Appendix Table S1) with the T7/T3 phage polymerase promoter added at the 5' end of the primer.
381 *COOLAIR* RNA was then generated by following a protocol provided by the MAXIscript® T7
382 Transcription Kit (Invitrogen). The resulting product was DNA digested, denatured, and separated on
383 5% TBE gel containing 8 M Urea. The band at the right size was cut out, sliced, and eluted in gel
384 extraction buffer (0.5 M NH4Ac, 1 mM EDTA, 0.2% SDS, 1xRNAsecure™ (Invitrogen)) at 37ºC
385 overnight, followed by precipitation with isopropanol. 10 pmol purified RNA was 3'biotinylated by
386 following the instructions provided by the RNA 3' End Biotinylation Kit (Pierce). The labelling
387 efficiency was determined to be at least 90%. For the gel shift assay, a 20 µl reaction (25 ng/µl protein,
388 2 nM probe, 250 ng/µl tRNA, 50 ng/µl heparin, 10 mM HEPES (pH 7.3), 120 mM KCL, 1 mM $MgCl_2$,
389 1 mM DTT) was set up on ice. For the competition assay, 2x to 100x of unlabelled probe was included
390 in the reaction. The reaction with only GST was used as a negative control. The mixture was incubated
391 at room temperature for 5 min and resolved on 3.5% native TBE-acrylamide gel and transferred onto a
392 positively charged nylon membrane. The biotinylated RNA on the membrane was detected by
393 chemiluminescence according to a protocol provided with the Chemiluminescent Nucleic Acid
394 Detection Module (Pierce, 89880). Primers to generate probes were listed below. For the binding
395 reaction, 1 µg of different recombinant proteins was incubated with 2 pmol of biotinylated probe in 20
396 µL of 1× buffer containing 20 mM Tris (pH 7.5), 100 mM NaCl, 10 mM $MgCl_2$, non-specific
397 competitors (1µg/µl heparin and 5µg tRNA) and 0.05% Triton X-100 at room temperature for 10 min.
398 The RNA-protein mixture was resolved on 6% 1× TBE acrylamide gel under 100 V for 50 min,
399 followed by electrophoretic transfer to positively charged nylon membranes (GE Healthcare). The
400 biotinylated RNA on the membrane was UV cross-linked and detected using chemiluminescent nucleic
401 acid detection following the manufacturer's instructions (Thermo).
402
403 **Acknowledgements**
404 We thank Shuqin Chen and Tina Zhang for their excellent technical assistance and Hsuan Pai for her
405 artwork assistance. We also thank all members of the Dean and Howard groups. This work was
406 funded by the European Research Council Advanced Grant (EPISWITCH, 833254), Wellcome Trust

(210654/Z/18/Z), and the Royal Society Professorship (RP\R1\180002) to Caroline Dean, and EPSRC grants (EP/T00214X/1 to C.D. and EP/T002166/1 and EP/W024063/1 to M.L).

Author contributions

G-J.J. and C.D. conceived the study. G-J.J., A.P.-D., R.M., Z.W., F.L. and S.G.L. performed the investigation and analysed the data. G-J.J. and C.D. wrote the manuscript; all authors reviewed and edited the manuscript. M.C.L. and C.D. supervised the study, acquired the funding, and were the project administrators.

References

Amara U, Hu J, Cai J & Kang H (2023) FLK is an mRNA m6A reader that regulates floral transition by modulating the stability and splicing of FLC in Arabidopsis. *Mol Plant* 16: 919–929

Banani SF, Lee HO, Hyman AA & Rosen MK (2017) Biomolecular condensates: Organizers of cellular biochemistry. *Nat. Rev. Mol. Cell Biol.* 18: 285-298

Bayle V, Fiche JB, Burny C, Platre MP, Nollmann M, Martinière A & Jaillais Y (2021) Single-particle tracking photoactivated localization microscopy of membrane proteins in living plant tissues. *Nat Protoc* 16: 1600–1628

Berry S, Rosa S, Howard M, Bühler M & Dean C (2017) Disruption of an RNA-binding hinge region abolishes LHP1-mediated epigenetic repression. *Genes Dev* 31: 2115–2120

Bindels DS, Haarbosch L, Van Weeren L, Postma M, Wiese KE, Mastop M, Aumonier S, Gotthard G, Royant A, Hink MA, *et al* (2016) mScarlet: A bright monomeric red fluorescent protein for cellular imaging. *Nat Methods* 14: 53–56

Biswas S, Chen Z, Karslake JD, Farhat A, Ames A, Raiymbek G, Freddolino PL, Biteen JS & Ragunathan K (2022) HP1 oligomerization compensates for low-affinity H3K9me recognition and provides a tunable mechanism for heterochromatin-specific localization. *Sci Adv* 8

Dobin A, Davis CA, Schlesinger F, Drenkow J, Zaleski C, Jha S, Batut P, Chaisson M & Gingeras TR (2013) STAR: Ultrafast universal RNA-seq aligner. *Bioinformatics* 29: 15–21

Chakrabortee S, Kayatekin C, Newby GA, Mendillo ML, Lancaster A & Lindquist S (2016) Luminidependens (LD) is an Arabidopsis protein with prion behavior. *Proc Natl Acad Sci U S A* 113: 6065–6070

Cho WK, Spille JH, Hecht M, Lee C, Li C, Grube V & Cisse II (2018) Mediator and RNA polymerase II clusters associate in transcription-dependent condensates. *Science* 361: 412–415

Fang X, Wang L, Ishikawa R, Li Y, Fiedler M, Liu F, Calder G, Rowan B, Weigel D, Li P, *et al* (2019) Arabidopsis FLL2 promotes liquid–liquid phase separation of polyadenylation complexes. *Nature* 569: 265–269

Fang X, Wu Z, Raitskin O, Webb K, Voigt P, Lu T, Howard M & Dean C (2020) The 3 processing of antisense RNAs physically links to chromatin-based transcriptional control. *Proc Natl Acad Sci U S A* 117: 15316–15321

Fiedler M, Franco-Echevarría E, Schulten A, Nielsen M, Rutherford TJ, Yeates A, Ahsan B, Dean C & Bienz M (2022) Head-to-tail polymerization by VEL proteins underpins cold-induced Polycomb silencing in flowering control. *Cell Rep* 41

Field S, Jang GJ, Dean C, Strader LC & Rhee SY (2023) Plants use molecular mechanisms mediated by biomolecular condensates to integrate environmental cues with development. *Plant Cell* 35: 3173–3186

Henderson IR, Liu F, Drea S, Simpson GG & Dean C (2005) An allelic series reveals essential roles for FY in plant development in addition to flowering-time control. *Development* 132: 3597–3607

Izeddin I, Récamier V, Bosanac L, Cissé II, Boudarene L, Dugast-Darzacq C, Proux F, Bénichou O, Voituriez R, Bensaude O, *et al* (2014) Single-molecule tracking in live cells reveals distinct target-search strategies of transcription factors in the nucleus. *Elife* 2014: 1–27

456 Jin X, Lee JE, Schaefer C, Luo X, Wollman AJM, Payne-Dwyer AL, Tian T, Zhang X, Chen X, Li Y,
457 *et al* (2021) Membraneless organelles formed by liquid-liquid phase separation increase bacterial
458 fitness. *Sci Adv* 7
459 Jumper J, Evans R, Pritzel A, Green T, Figurnov M, Ronneberger O, Tunyasuvunakool K, Bates R,
460 Žídek A, Potapenko A, *et al* (2021) Highly accurate protein structure prediction with AlphaFold.
461 *Nature* 596: 583–589
462 Kent S, Brown K, Yang C hsun, Alsaihati N, Tian C, Wang H & Ren X (2020) Phase-Separated
463 Transcriptional Condensates Accelerate Target-Search Process Revealed by Live-Cell Single-
464 Molecule Imaging. *Cell Rep* 33: 108248
465 Ladouceur AM, Parmar BS, Biedzinski S, Wall J, Tope SG, Cohn D, Kim A, Soubry N, Reyes-
466 Lamothe R & Weber SC (2020) Clusters of bacterial RNA polymerase are biomolecular
467 condensates that assemble through liquid-liquid phase separation. *Proc Natl Acad Sci U S A* 117:
468 18540–18549
469 Leake MC, Wilson D, Bullard B, Simmons RM & Bubb MR (2003) The elasticity of single kettin
470 molecules using a two-bead laser-tweezers assay. *FEBS Lett* 535: 55–60
471 Leake MC, Chandler JH, Wadhams GH, Bai F, Berry RM & Armitage JP (2006) Stoichiometry and
472 turnover in single, functioning membrane protein complexes. *Nature* 443: 355–358
473 Leake MC, Greene NP, Godun RM, Granjon T, Buchanan G, Chen S, Berry RM, Palmer T & Berks
474 BC (2008) Variable stoichiometry of the TatA component of the twin-arginine protein transport
475 system observed by in vivo single-molecule imaging. *Proc Natl Acad Sci U S A* 105: 15376–15381
476 Leake MC (2014) Analytical tools for single-molecule fluorescence imaging in cellulo. *Phys Chem*
477 *Chem Phys* 16: 12635–12647
478 Liu F, Quesada V, Crevillén P, Bäurle I, Swiezewski S & Dean C (2007) The Arabidopsis RNA-
479 Binding Protein FCA Requires a Lysine-Specific Demethylase 1 Homolog to Downregulate FLC.
480 *Mol Cell* 28: 398–407
481 Liu F, Marquardt S, Lister C, Swiezewski S & Dean C (2010) Targeted 3′ processing of antisense
482 transcripts triggers arabidopsis FLC chromatin silencing. Macknight R, Bancroft I, Page T, Lister
483 C, Schmidt R, Love K, Westphal L, Murphy G, Sherson S, Cobbett C, *et al* (1997) FCA, a gene
484 controlling flowering time in arabidopsis, encodes a protein containing RNA-binding domains.
485 *Cell* 89: 737–7
486 Mateo-Bonmatí E, Montez M, Maple R, Fiedler M, Fang X, Saalbach G, Passmore LA & Dean CA
487 (2024) A CPF-like phosphatase module links transcription termination to chromatin silencing.
488 *bioRxiv*: 2023.07.06.547976
489 Payne-Dwyer AL & Leake MC (2022) Single-molecular quantification of flowering control proteins
490 within nuclear condensates in live whole Arabidopsis root. *Methods in Molecular Biology* 2476:
491 311-328.
492 Payne-Dwyer AL, Syeda AH, Shepherd JW, Frame L & Leake MC (2022) RecA and RecB: Probing
493 complexes of DNA repair proteins with mitomycin C in live Escherichia coli with single-molecule
494 sensitivity. *J R Soc Interface* 19
495 Payne-Dwyer A, Kumar G, Barrett J, Gherman LK, Hodgkinson M, Plevin M, Mackinder L, Leake
496 MC & Schaefer C (2023) Predicting Rubisco:Linker Condensation from Titration in the Dilute
497 Phase. arXiv:2301.05681
498 Plank M, Wadhams GH & Leake MC (2009) Millisecond timescale slimfield imaging and automated
499 quantification of single fluorescent protein molecules for use in probing complex biological
500 processes. *Integr Biol* 1: 602–612
501 Quesada V, Macknight R, Dean C & Simpson GG (2003) Autoregulation of FCA pre-mRNA
502 processing controls Arabidopsis flowering time. *EMBO J* 22: 3142–3152
503 Qüesta JI, Song J, Geraldo N, An H & Dean C (2016) Arabidopsis transcriptional repressor VAL1
504 triggers Polycomb silencing at *FLC* during vernalization. Science 353: 485–488
505 Reyes-Lamothe R, Sherratt DJ & Leake MC (2010) Stoichiometry and architecture of active DNA
506 replication machinery in escherichia coli. *Science* 328: 498–501
507 Rosa S, De Lucia F, Mylne JS, Zhu D, Ohmido N, Pendle A, Kato N, Shaw P & Dean C (2013)
508 Physical clustering of FLC alleles during polycomb-mediated epigenetic silencing in vernalization.
509 *Genes Dev* 27: 1845–1850
510 Rosa S, Duncan S & Dean C (2016) Mutually exclusive sense-antisense transcription at *FLC*

511 facilitates environmentally induced gene repression. *Nat Commun* 7: 1–7
512 Ruff KM, Dar F & Pappu R V. (2021) Ligand effects on phase separation of multivalent
513 macromolecules. *Proc Natl Acad Sci U S A* 118
514 Shen Z, Jia B, Xu Y, Wessén J, Pal T, Chan HS, Du S & Zhang M (2023) Biological condensates
515 form percolated networks with molecular motion properties distinctly different from dilute
516 solutions. *Elife* 12: 1–32
517 Shin Y & Brangwynne CP (2017) Liquid phase condensation in cell physiology and disease. *Science*
518 357
519 Simpson GG, Dijkwel PP, Quesada V, Henderson I & Dean C (2003) FY is an RNA 3′ end-
520 processing factor that interacts with FCA to control the Arabidopsis floral transition. *Cell* 113:
521 777–787
522 Simpson GG, Laurie RE, Dijkwel PP, Quesada V, Stockwell PA, Dean C & Macknight RC (2010)
523 Noncanonical translation initiation of the Arabidopsis flowering time and alternative
524 polyadenylation regulator FCA. *Plant Cell* 22: 3764–3777
525 Soller M & White K (2005) ELAV Multimerizes on Conserved AU 4–6 Motifs Important for. *Society*
526 25: 7580–7591
527 Sonmez C, Bäurle I, Magusin A, Dreos R, Laubinger S, Weigel D & Dean C (2011) RNA 3′
528 processing functions of Arabidopsis FCA and FPA limit intergenic transcription. P*roc Natl Acad*
529 *Sci U S A* 108: 8508–8513
530 Syeda AH, Wollman AJM, Hargreaves AL, Howard JAL, Bruning JG, McGlynn P & Leake MC
531 (2019) Single-molecule live cell imaging of Rep reveals the dynamic interplay between an
532 accessory replicative helicase and the replisome. *Nucleic Acids Res* 47: 6287–6298
533 Sun B, Bhati KK, Song P, Edwards A, Petri L, Kruusvee V, Blaakmeer A, Dolde U, Rodrigues V,
534 Straub D, *et al* (2022) FIONA1-mediated methylation of the 3'UTR of *FLC* affects *FLC* transcript
535 levels and flowering in Arabidopsis. *PLoS Genet* 18: 1–22
536 Varadi M, Anyango S, Deshpande M, Nair S, Natassia C, Yordanova G, Yuan D, Stroe O, Wood G,
537 Laydon A, *et al* (2022) AlphaFold Protein Structure Database: Massively expanding the structural
538 coverage of protein-sequence space with high-accuracy models. *Nucleic Acids Res* 50: D439–
539 D444
540 Wang C, Yang J, Song P, Zhang W, Lu Q, Yu Q & Jia G (2022) FIONA1 is an RNA N 6-
541 methyladenosine methyltransferase affecting Arabidopsis photomorphogenesis and flowering.
542 *Genome Biol* 23: 1–29
543 Wadsworth GM, Zahurancik WJ, Zeng X, Pullara P, Lai LB, Sidharthan V, Pappu R V., Gopalan V &
544 Banerjee PR (2023) RNAs undergo phase transitions with lower critical solution temperatures. *Nat*
545 *Chem* 15: 1693–1704
546 Wollman AJM & Leake MC (2015) Millisecond single-molecule localization microscopy combined
547 with convolution analysis and automated image segmentation to determine protein concentrations
548 in complexly structured , functional cells , one cell at a time. *Faraday Discuss* 00: 1–24
549 Wollman AJM, Shashkova S, Hedlund EG, Friemann R, Hohmann S & Leake MC (2017)
550 Transcription factor clusters regulate genes in eukaryotic cells. *Elife* 6: 1–36
551 Xu C, Wu Z, Duan HC, Fang X, Jia G & Dean C (2021) R-loop resolution promotes co-
552 transcriptional chromatin silencing. *Nat Commun* 12
553 Yongke Tlan, Zheng Han, Zhang Fel, Wang Shillang, Ji Xiaoru, Xu Chao, He Yuehul & Ding Yong
554 (2019) PRC2 recruitment and H3K27me3 deposition at *FLC* require FCA binding of *COOLAIR*.
555 *Sci Adv* 5: 1–12
556 Zhu P, Lister C & Dean C (2021) Cold-induced Arabidopsis FRIGIDA nuclear condensates for *FLC*
557 repression. *Nature* 599: 657–661
558

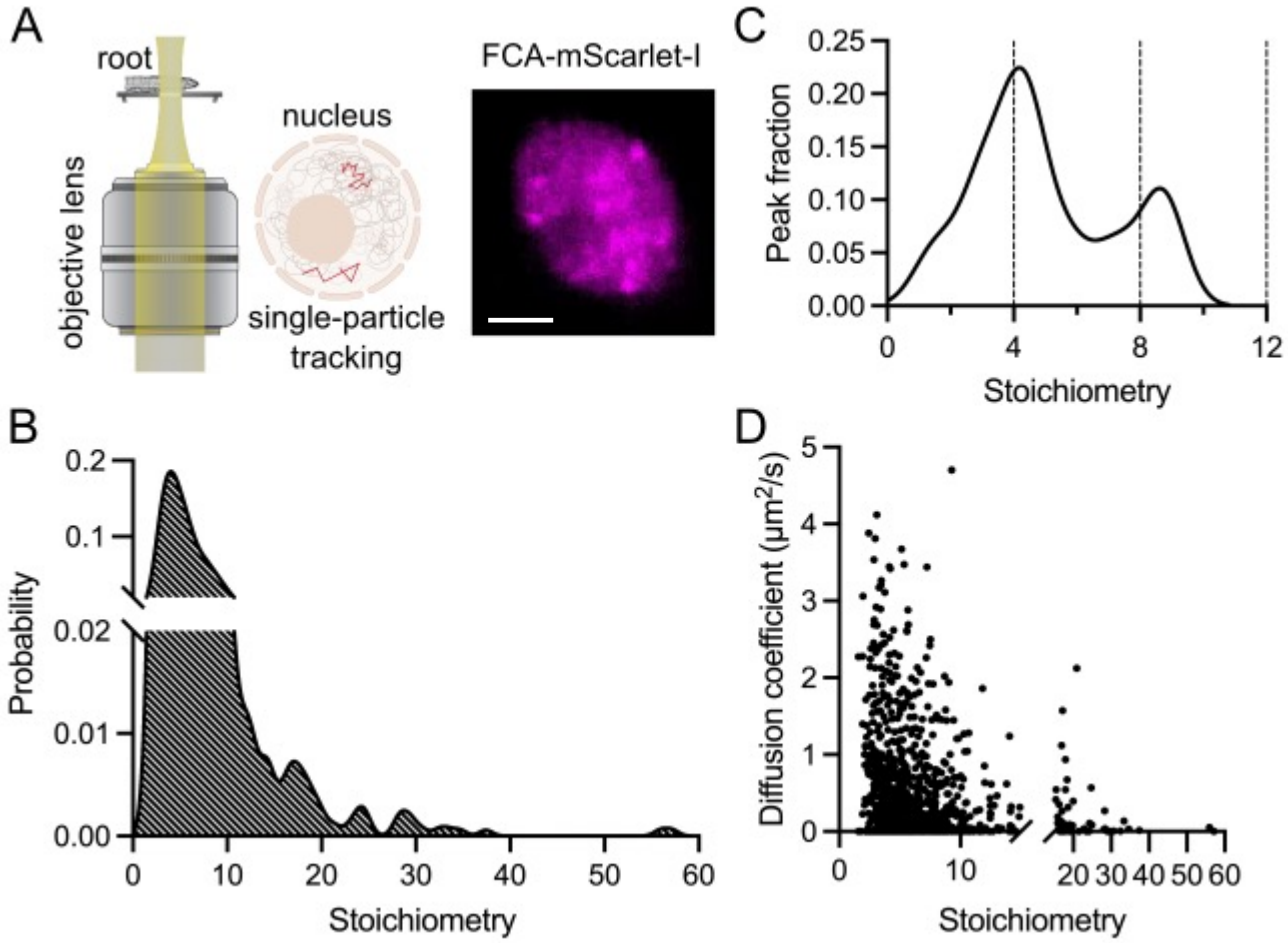

Figure 1. Super-resolution and single-particle tracking characterize physical properties of FCA condensates

A SlimVar microscopy of FCA-mScarlet-I (in magenta) in Arabidopsis root cells. Scale bar, 2 μm.

B Distributions of stoichiometry (molecule number) of individual FCA particles.

C Periodicity of FCA particle stoichiometry estimated from the most common spacing between neighboring peaks in each stoichiometry distribution.

D The diffusion coefficient and stoichiometry of each FCA particles.

The single-particle tracking analysis is from 3 biologically independent experiments. Results from individual replicate are provided in Appendix Figure S1.

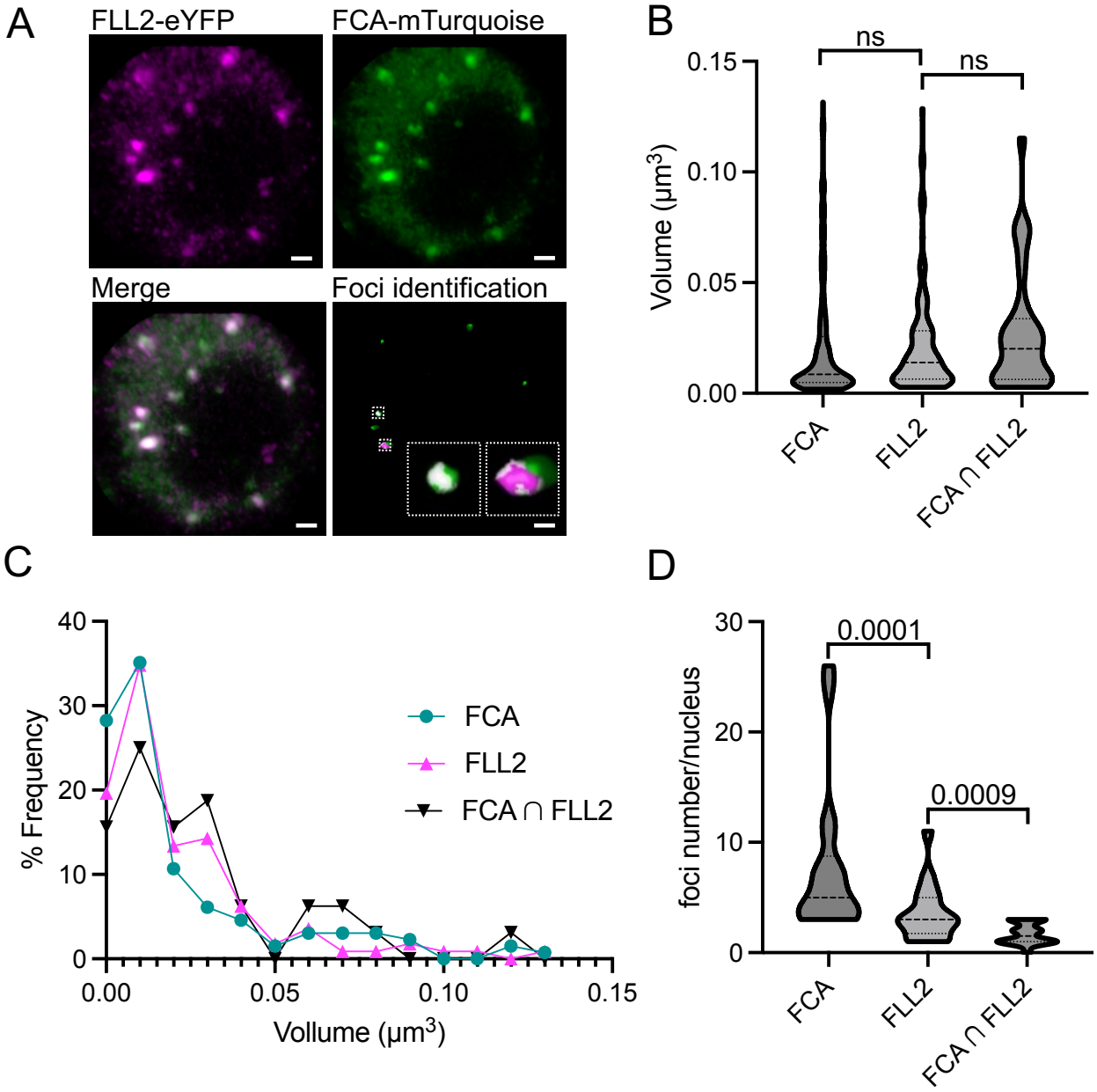

Figure 2. The co-localization of FCA and FLL2 is primarily observed in a limited number of prominent foci in Arabidopsis

A Representative 3D images of FCA and FLL2 colocalization. The FCA were identified and labelled in green and FLL2 labelled in magenta using Vision4D software. White labelling indicates the co-localization of FCA with FLL2. The enlarged images of co-localized foci were shown in insets at the bottom right corner. Scale bars, 1 μm.

B Quantification of size of identified FCA, FLL2 and co-localized foci. The lines in the violin plots indicate the median and quartiles. ns, no significance.

C Size and frequency distribution of FCA, FLL2 and co-localized foci.

D Number of FCA, FLL2 or co-localized foci in each nuclei. The lines in the violin plots indicate the median and quartiles. Non-parametric Brunner-Munzel test.

The quantitative analysis is based on 18 nuclei from 5 independent samples in 1 representative replicate. The labeled P-value was analyzed using the non-parametric Brunner-Munzel test.

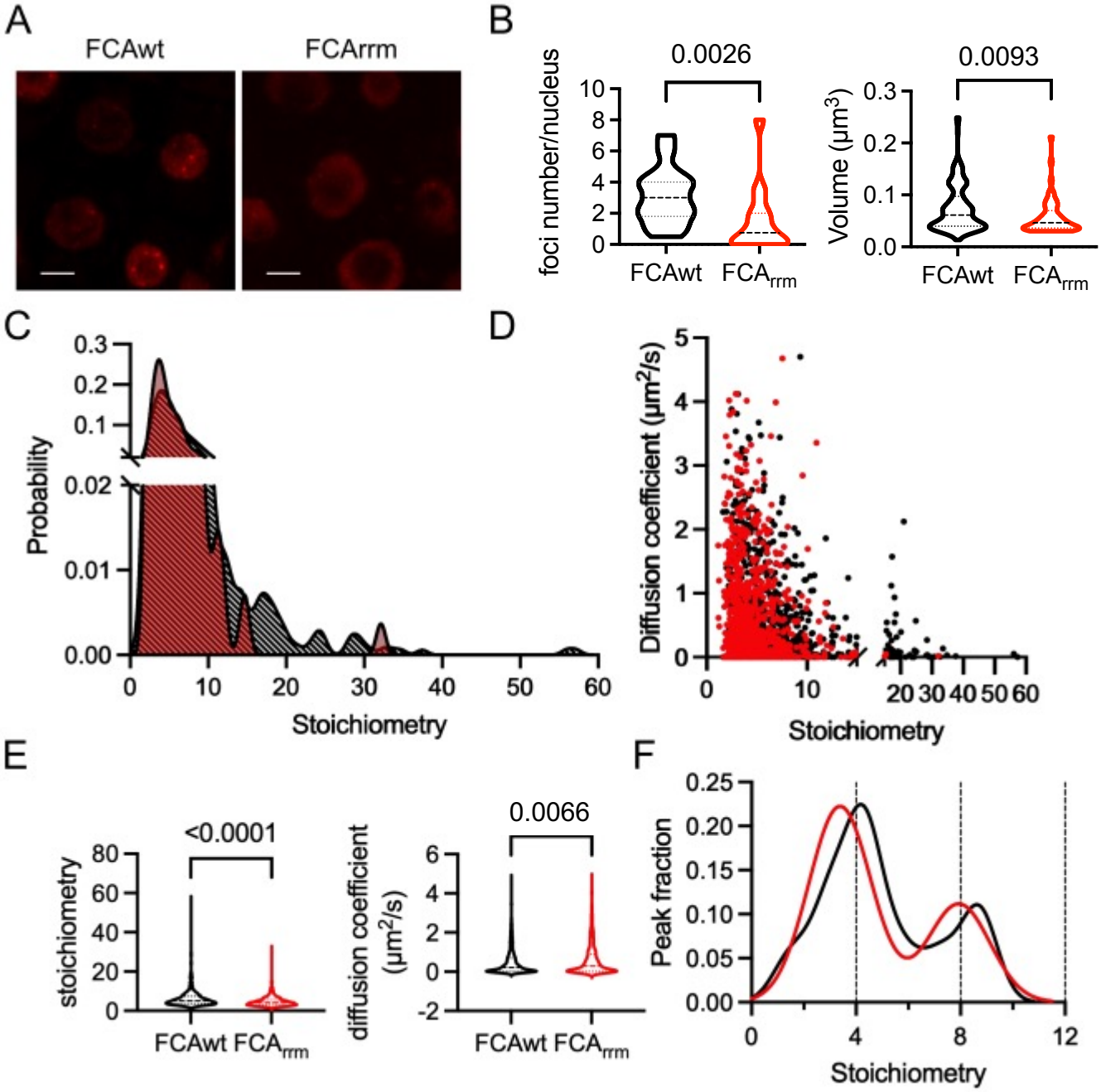

Figure 3. The RNA-binding activity of FCA modulates FCA condensates

A Representative Airyscan confocal images of wild type FCA fused mScarlet-I (FCAwt) and FCA with L304F mutation (FCArrm). Scale bars, 5 μm.

B Quantification of size and number of FCAwt and FCArrm condensates using Vision4D software. The lines in the violin plots indicate the median and quartiles. The quantitative analysis is based on 43 FCAwt nuclei and 65 FCArrm nuclei from 3 independent experiments.

C Distributions of stoichiometry of individual FCAwt (in black) and FCArrm (in red) particles.

D The diffusion coefficient and stoichiometry of each FCAwt (in black) and FCArrm (in red) particles.

E Statistic analysis of stoichiometry and diffusion coefficient of FCAwt and FCArrm particles.

F Periodicity of FCAwt (in black) and FCArrm (in red) particle stoichiometry.

The single-particle tracking analysis is from 3 biologically independent experiments. The FCAwt data corresponds to that shown in Figure 1. The labeled P-value was analyzed using the non-parametric Brunner-Munzel test. Results from individual replicate are provided in Appendix Figure S1 and S3.

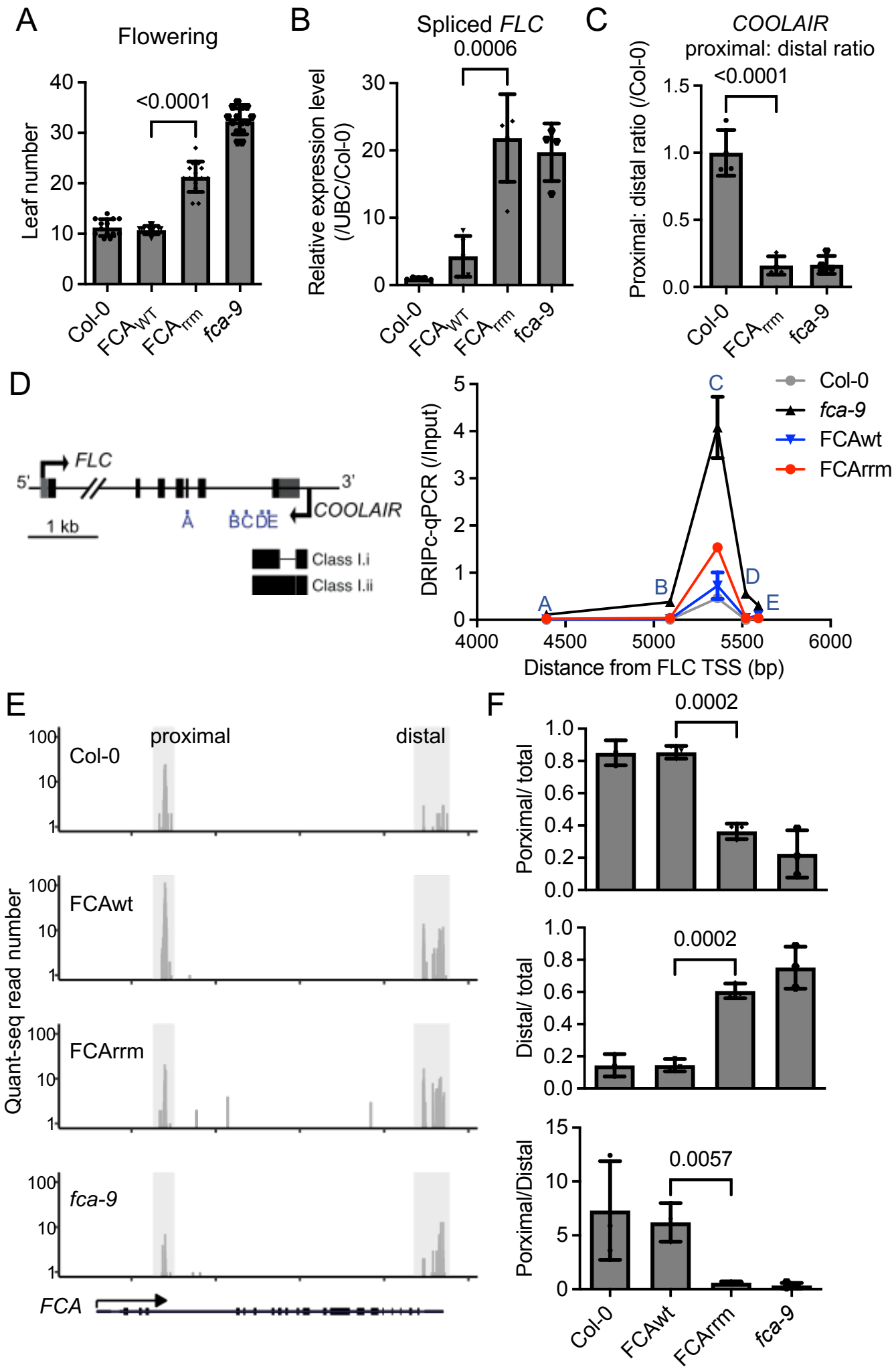
A
Flowering
Leaf number
<0.0001
Col-0
FCAWT
FCArrm
fca-9
B
Spliced FLC
0.0006
Relative expression level (/UBC/Col-0)
C
COOLAIR
proximal: distal ratio
<0.0001
Proximal: distal ratio (/Col-0)
D
FLC
5'
3'
1 kb
COOLAIR
Class I.i
Class I.ii
DRIPc-qPCR (/Input)
Distance from FLC TSS (bp)
Col-0
fca-9
FCAwt
FCArrm
E
proximal
distal
Col-0
FCAwt
FCArrm
fca-9
Quant-seq read number
FCA
F
0.0002
Porximal/ total
0.0002
Distal/ total
0.0057
Porximal/Distal
Col-0
FCAwt
FCArrm
fca-9

Figure 4. The missense mutation in the RRM of FCA only partially complements the *fca-9* mutant phenotype

A Flowering time of indicated plants grown in long-day photoperiod. Data are presented as mean ± s.d. (n = 10).

B Expression of spliced *FLC* relative to *UBC* in the indicated plants. Data are presented as mean ± s.d. (n = 5).

C The level of proximal isoforms of *COOLAIR* transcripts in the indicated plants relative to control (FCAwt). Data are presented as mean ± s.d. (n = 4).

D DRIPc–qPCR analyzing *COOLAIR* R-loop in indicated plants. Data are mean ± s.d. from one representative replicate of three biological replicates.

E Quant-seq experiment results from the *FCA* locus carried out on indicated seedlings. The vertical pale gray bars highlight proximal and distal polyA sites.

F Quantification of reads corresponding to proximal and distal polyadenylated *FCA* transcripts. Data are presented as mean ± s.d. (n = 3).

The labeled P-value was analyzed using the two-tailed t-test.